Dalton Transactions

ROYAL SOCIETY OF CHEMISTRY

PAPER

View Article Online
View Journal | View Issue

Cite this: *Dalton Trans.*, 2023, **52**, 16189

Oxygen-carrying acid-responsive Cu/ZIF-8 for photodynamic antibacterial therapy against cariogenic *Streptococcus mutans* infection†

Ruifeng Wang,‡[a,c] Qiyuan Pan,‡[a] Fang Li,[a] Jingying Guo,[a] Yaru Huo,[a] Chao Xu,[a] Manwen Xiong,[a] Ziyong Cheng,[d] Min Liu*[a] and Jun Lin *[b]

Caries as a result of acid demineralization is the most common oral microbial infectious disease. Due to the small and complex intraoral operating space, it is challenging to completely remove *Streptococcus mutans* (*S. mutans*) and other cariogenic bacteria. As an intelligent acid-responsive photosensitive nanomaterial, O_2-Cu/ZIF-8@Ce6/ZIF-8@HA (OCZCH) was chosen to adapt to the anaerobic and acidic microenvironment for inactivating *S. mutans*. In this work, OCZCH not only exhibits a regular nanomorphology in SEM and TEM images but also shows intelligent acid responsiveness as evidenced by the release of Ce6 and oxygen. When excited by near-infrared light at 650 nm, Ce6 releases reactive oxygen species (ROS) that act synergistically with internal oxygen to significantly enhance the antimicrobial therapeutic effect of photodynamic therapy (PDT). *In vitro* antimicrobial experiments showed that OCZCH could achieve an impressive sterilization effect against *S. mutans* and biofilm. Notably, the acid-producing ability of the bacteria was also significantly inhibited. With its oxygen-carrying photosensitizing properties, excellent responsiveness to acidic environments, and antimicrobial capacity under anaerobic conditions, OCZCH is considered an innovative candidate for clinical application in treating dental caries.

Received 30th August 2023,
Accepted 4th October 2023

DOI: 10.1039/d3dt02816j

rsc.li/dalton

Introduction

Carbohydrates retained on the dental surface serve as a source of nutrients that are utilized by the plaque biofilm for acid fermentation, which alters the oral microenvironment. As a result of continued bacterial acid production, healthy teeth will progress through hard tissue demineralization to irreversible caries.[1,2] *Streptococcus mutans* (*S. mutans*) is considered an indispensable bacterium in the development of dental caries due to its extraordinary cariogenicity, such as acid production, acid resistance, and exopolysaccharide (EPS) production.[3,4] The EPS secreted by *S. mutans* mediates bacterial adhesion to the tooth surface, creating a favourable anaerobic environment for cariogenic bacteria reproduction and the promotion of biofilm formation.[5–7] Therefore, an effective strategy to inhibit the viability of *S. mutans* and its biofilm formation is crucial for the prevention and treatment of caries.

The application of dental handpieces to remove decayed dentin and replace it with restorative materials is the most common repair strategy.[8] However, the mechanical treatment process brings fear and pain to the patient and the complete removal of carious dentin close to the dental pulp presents a serious challenge.[9] What's more, the use of antibiotics poses a certain risk as it disturbs the balance of normal oral flora and leads to bacterial antibiotic resistance.[10] In contrast to traditional therapy, photodynamic therapy (PDT) seems like a gentle alternative to overcome the defects of discomfort and drug resistance. When exposed to specific wavelengths of light, photosensitizers (PS), such as chlorin e6 (Ce6), generate reactive oxygen species (ROS) in an oxygen-rich environment. The high cytotoxicity of ROS kills bacteria unselectively *via* an oxidative burst.[11,12] Therefore, PDT has been generally recognized as a promising antimicrobial strategy.[13] Many photosensitizers have been widely used in photodynamic antimicrobial therapy due to their good photo-responsiveness, such as indocyanine green (ICG) and curcumin.[14–17] As a second-generation chlorophyll-related photosensitizer, Ce6 not only exhibits

[a]*Department of Periodontology, Hospital of Stomatology, Jilin University, Changchun 130021, China. E-mail: liu_min99@jlu.edu.cn*
[b]*State Key Laboratory of Rare Earth Resource Utilization, Changchun Institute of Applied Chemistry, Chinese Academy of Sciences, Changchun, 130022, China. E-mail: jlin@ciac.ac.cn*
[c]*Weihai Stomatological Hospital, Weihai 264200, China*
[d]*Key Laboratory of Superlight Materials and Surface Technology, Ministry of Education, College of Materials Science and Chemical Engineering, Harbin Engineering University, Harbin 150001, China*
† Electronic supplementary information (ESI) available: Addition of experimental details, XPS spectra, UV–vis absorption spectra of DPBF, cell viability test, BET, *etc*. See DOI: https://doi.org/10.1039/d3dt02816j
‡ These authors contributed equally to this work.

excellent photodynamic activity with a strong absorption peak under red light (600–700 nm) but also has advantages such as high singlet oxygen ($^1O_2$) yield, low dark toxicity, and stable chemical properties. However, the planar conjugated structure required for light absorption by photosensitizers results in a hydrophobic Ce6 molecule that tends to agglomerate under physiological conditions, severely limiting photodynamic efficiency.[18] To overcome these issues, researchers choose to encapsulate PS with nanocarriers in most cases.[19,20]

Zeolitic imidazolate framework-8 (ZIF-8) is a recognized nanocarrier that consists of zinc ions (Zn^{2+}) and 2-methylimidazole (2-MI). As a type of metal–organic backbone material (MOF), ZIF-8 has organic and inorganic properties such as pH-responsiveness, good biocompatibility, porousness, and the potential to carry drugs and gases.[21,22] Additionally, Ce6 can be easily loaded into ZIF-8 through electrostatic adsorption by Zn^{2+}.[8] As one of the most representative nanocarriers in the biomedical field, ZIF-8 not only degrades and releases photosensitizers in acidic environments, but also carries oxygen to solve problems such as biofilm hypoxia and oxygen depletion.[23] However, the oxygen-carrying capacity is lower than that of copper-doped MOFs.[24,25] Given this, we synthesized Cu/ZIF-8 by doping ZIF-8 with copper, which increases the O_2 storage capacity.[26] Copper nanoparticles show excellent antibacterial abilities against both Gram-positive and Gram-negative bacteria,[27,28] but the cytotoxicity of Cu^{2+} is not negligible. Therefore, hyaluronic acid (HA) was added to the outermost layer of nanoparticles to enhance their biocompatibility.

Based on the aforementioned background, we prepared O_2-Cu/ZIF-8@Ce6/ZIF-8@HA (OCZCH) as an acid and light-responsive PDT nanosystem that met our expectations. To overcome the problem of microenvironmental hypoxia, we first prepared oxygen-loaded Cu^{2+}-doped ZIF-8 (Cu/ZIF-8) and then synthesized a layer of Ce6-containing ZIF-8 on its surface; finally, HA wrapped in the outermost layer. This nanosystem not only solves the problem of Ce6 agglomeration under physiological conditions but also addresses the inefficiency of PDT caused by microenvironmental hypoxia within the plaque biofilm and continuous oxygen consumption during photodynamic therapy. Within the acidic *S. mutans* plaque biofilm, the OCZCH structure disintegrates rapidly with O_2 releasing from it. Upon the enhancement of O_2, Ce6 generates a large amount of ROS to inactivate bacteria under 650 nm laser irradiation. This nanosystem significantly enhances the efficiency of PDT and results in the inactivation of *S. mutans*. Therefore, OCZCH is deemed suitable for clinical application in treating bacteriogenic caries.

Results and discussion

Preparation and characterization of OCZCH

ZIF-8, Cu/ZIF-8, O_2-Cu/ZIF-8@Ce6/ZIF-8 (OCZC), and OCZCH nanoparticles were synthesized by assembling components in a methanol solution and then stirring at room temperature in the dark (Fig. 1). Methanol was chosen as the solvent for the experimental reactions because of its volatility and easy removal from the nanopores by vacuum drying, allowing for subsequent oxygen storage. At the same time, the Cu/ZIF-8@Ce6/ZIF-8 (CZC) and Cu/ZIF-8@Ce6/ZIF-8@HA (CZCH) groups synthesized without oxygen input were involved in the follow-up experiment as the control group. The structure of the reaction products was observed using TEM and SEM (Fig. 2a and b), showing regular dodecahedral crystals with a uniform 170 nm particle size. The element mapping of OCZCH shows that the elements C, N, Cu, Zn, and O are uniformly distributed in the nanoparticle structure (Fig. 2c). Through the peaks of XRD (Fig. 2d), we found that the prepared ZIF-8 has the

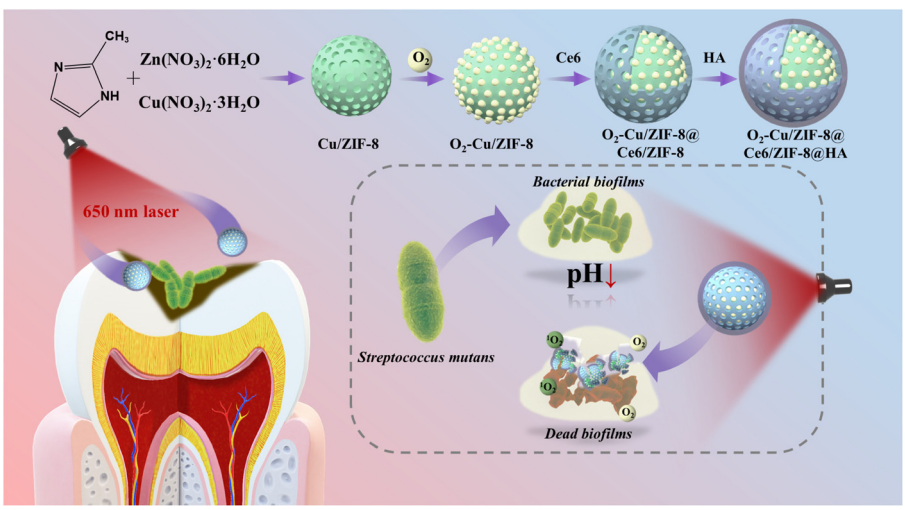

Fig. 1 Schematic illustration of the OCZCH nanoparticles' fabrication and the mechanism for inactivating cariogenic bacteria with acid responsiveness under near-infrared light. OCZCH NPs were prepared *via* assembling Zn^{2+} and Cu^{2+} ions with 2-methylimidazole. Ce6 and hyaluronic acid were further modified. Once exposed to an acidic microenvironment, pH-sensitive OCZCH NPs release oxygen and Ce6 in response to near-infrared light with ROS generation. The abundant ROS can inactivate *S. mutans* bacteria and destroy cariogenic biofilms.

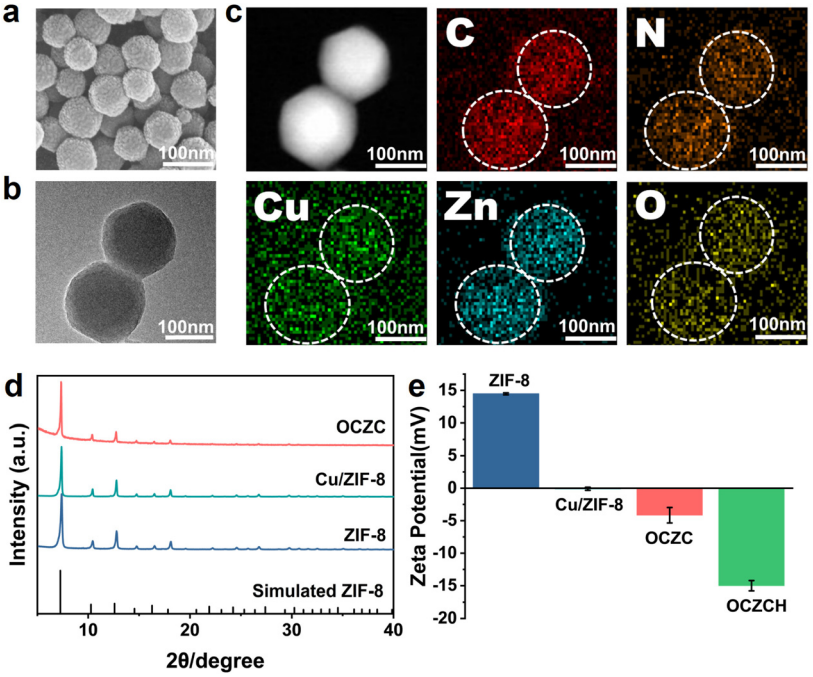

Fig. 2 Materials characterization. (a) SEM image. (b) TEM image. (c) High-angle annular dark-field scanning TEM (HAADF-STEM) image and the element mappings of OCZCH including Cu, Zn, C, N, and O. (d) X-ray diffraction (XRD) patterns of OCZC, Cu/ZIF-8, and ZIF-8. (e) The zeta potentials of ZIF-8, Cu/ZIF-8, OCZC and OCZCH.

same X-ray diffraction peaks as that in the previous report,[25] which means the same crystal structure. The X-ray photoelectron spectroscopy (XPS) results demonstrate the existence of Zn and Cu in Cu/ZIF-8. A clear Zn 2p electron energy spectrum is shown in Fig. S1a.† The peaks in Fig. S1b† at 932.4 eV and 952.1 eV belong to the Cu 2p3/2 and Cu 2p1/2 electron energy spectra of Cu^{2+} respectively. In addition to the above characterization, the zeta potential in Fig. 2e shows a distinctive decrease after the nanomaterials have been modified with HA. This decrease is attributed to the plentiful negatively charged carboxyl groups of HA, which have a coordinating effect with the Zn^{2+} in the material, thus neutralizing some of the positive charges and leading to a decrease in potential.[29–31] All of the above results indicate the successful preliminary synthesis of the nanomaterials.

Carrying capacity and acid responsiveness of OCZCH

To improve the loadability, we prepared Cu/ZIF-8 with a 25% Cu feed ratio based on the previous literature.[25] The oxygen adsorption isotherm (Fig. 3a) shows that at the same atmospheric pressure, ZIF-8 has an oxygen-carrying capacity of 2.45 cc g^{-1} while Cu/ZIF-8 reaches 4.69 cc g^{-1}. It is easy for us to conclude that the oxygen storage capacity of Cu/ZIF-8 is approximately doubled due to the addition of Cu. These results all mean that Cu/ZIF-8 is an efficient oxygen-carrying carrier that can provide sufficient oxygen to enhance later photodynamic antibacterial action.

Ce6 was loaded into the Cu/ZIF-8 shell layer using the one-pot method. The microporous structure is the basis for drug loading within ZIF-8. As shown in the nitrogen adsorption/desorption curves (Fig. 3b and c), there is an almost linear increase in the adsorption curve in the region of low relative pressure (P/P_0 < 0.05) and a rapid increase in adsorption volume, exhibiting a type I microporous adsorption curve.[24] These curves of ZIF-8 and CZC confirm the presence of a microporous structure. In addition to the above, the decrease in surface area, pore volume, and pore size of CZC after the encapsulation of Ce6 means the physical adsorption of Ce6 on the surface of ZIF-8 and occupation of part of the pore channel of ZIF-8 (Table S1†). We further compared the UV–vis spectra of Ce6, Cu/ZIF-8, and OCZC. As presented in Fig. 3d, pure Ce6 and OCZCH have characteristic absorption peaks at 400 nm and 660 nm,[32] while Cu/ZIF-8 has no obvious characteristic absorption peaks. The red-shifted Soret band at 400 nm and the blue-shifted Q band at 660 nm of OCZC can be attributed to the insertion of Zn^{2+} into the dihydroporphyrin ring of Ce6. The above experiments proved that Ce6 was successfully loaded. In addition, the NPs' colour changed during their synthesis. The methanol solution of Ce6, Cu/ZIF-8, and OCZC was dispersed in methanol as shown in the inset of Fig. 3d. Cu/ZIF-8 was whitish yellow, and the methanol solution of Ce6 was deep green, while the methanol solution of OCZC after encapsulation of the ZIF-8 shell containing Ce6 turned to grass green. The colour change of the material can most intuitively reflect the successful loading of Ce6 onto the material.

To determine the loading rate of Ce6 in OCZCH, the standard curve of Ce6 is first recorded. Fig. 3e shows the absorption peaks at 400 nm in a methanol solution of Ce6 with con-

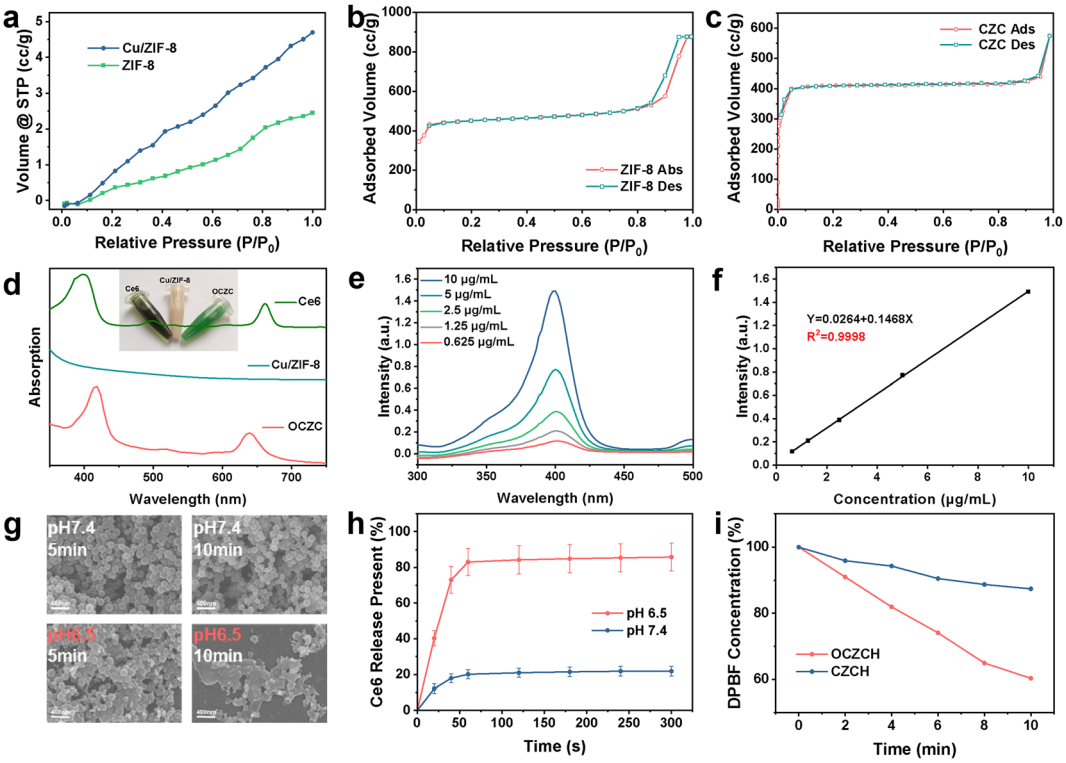

Fig. 3 (a) The oxygen adsorption isotherms of ZIF-8 and Cu/ZIF-8. Nitrogen adsorption/desorption curves of (b) ZIF-8 and (c) CZC. (d) Visual observation and the ultraviolet–visible (UV–vis) absorption spectra of Ce6, Cu/ZIF-8, and OCZC dissolved in methanol. (e) UV–vis absorption spectra of different concentrations of Ce6 in methanol solution. (f) Standard curve of Ce6. (g) SEM of OCZCH at pH 7.4 and pH 6.5 for 5 min or 10 min. (h) OCZCH was dispersed in phosphate-buffered saline (PBS) at pH 6.5 and 7.4. UV–vis absorption curves reflect the effect of pH on the release of Ce6 from OCZCH. (i) Change in the residual percentage of UV–vis absorption of DPBF over time.

centrations of 0.625, 1.25, 2.5, 5, and 10 μg mL^{-1}, respectively. According to the absorbance values of each concentration at 400 nm, the standard curve of Ce6 can be obtained by plotting a curve in Fig. 3f. The formula for plotting the Ce6 standard curve with a good linear relationship is $Y = 0.0264 + 0.1468X$ with $R^2 = 0.9998$. The loading percentage of Ce6 in OCZCH that was calculated from UV–vis absorption spectra is 3.2 wt%. Due to the caries microenvironment, it is necessary to investigate the degradation and functionality of materials under acidic conditions. The morphology and controlled-release behaviour of OCZCH nanoparticles in the acid microenvironment were revealed by SEM and UV–vis (Fig. 3g and h). To verify the excellent acid responsiveness of the nanoparticles, the obtained OCZCH was dispersed into phosphate-buffered saline (PBS) solutions with different pH values (7.4 and 6.5). As shown in Fig. 3g, the size of OCZCH nanoparticles remained well stabilized at pH 7.4. However, in a mildly acidic environment (pH 6.5) for 5 min, the OCZCH structure partially collapsed and gradually lost its regular ZIF-8 characteristic morphology. As time went on, the structure completely collapsed and disintegrated into tiny visible nanoparticles around it. Then, the release of Ce6 at different times was quantified according to the Ce6 standard curve (Fig. 3f and h). OCZCH was released rapidly in the first 30 s at pH 6.5, and the release curve levelled off after 60 s. The Ce6 release rate is up to 85.9% after the calculation. At the same time, the final release of OCZCH at pH 7.4 was only 21.8%. The above morphology and absorbance changes indicate that OCZCH can rapidly decompose and release the photosensitizer Ce6 in an acidic bacterial environment to facilitate the efficiency of PDT for antibacterial therapy. In addition to this, the stability of OCZCH under neutral conditions was also confirmed.

When irradiated by red light at 650 nm, Ce6 is capable of producing $^1O_2$, which plays an indispensable role in PDT. The biodegradation ability can be proved by the specific probe of $^1O_2$, DPBF. As shown in Fig. S2,† the absorption peak at 410 nm gradually decreased with the extension of time. The decrease in absorbance indicates that OCZCH produced an abundance of $^1O_2$ with increasing time. Upon comparing the percentage decrease in DPBF absorbance over 10 min between CZCH and OCZCH, we found that OCZCH produced four times more singlet oxygen in the presence of oxygen (Fig. 3i). This result indicates that more $^1O_2$ has been released and predicts the excellent antibacterial potential of OCZCH.

In vitro antimicrobial effects of OCZCH

Encouraged by well-controlled oxygen and Ce6 release in the acidic microenvironment, we further confirmed the PDT effect of OCZCH with an *in vitro* antibacterial assay. The minimum inhibitory concentration (MIC) is an index used to evaluate the

antibacterial activity of an antibacterial drug. It refers to the minimum drug concentration that can inhibit the growth of pathogenic bacteria in the culture medium after 18–24 hours of *in vitro* culture. The MIC of OCZCH against *S. mutans* was determined by a two-fold dilution method on an ultra-clean platform. As depicted in Fig. 4a, the solution became clear under 650 nm red light irradiation at OCZCH concentrations of 50 and 100 μg mL^{-1}. A CCK-8 experiment was conducted to verify the bio-safety of OCZCH (Fig. S3†). Different concentrations of OCZCH were co-cultured with L929, and the OD_{450} value proved the survival rate of the cell. There was no statistically significant difference between groups up to 50 μg mL^{-1}. Therefore, it should be taken for granted that OCZCH has good biocompatibility and can be used as a nanomedicine for a wider range of applications. Finally, 50 μg mL^{-1} was chosen as the concentration for subsequent experiments.

Only in living bacteria can the MTT be reduced by succinate dehydrogenase to water-insoluble blue-purple crystalline metazoan and deposited in the bacteria. Based on this principle, we used the MTT assay (Fig. 4b) to assess the effect of OCZCH on the metabolic activity of *S. mutans*. The inhibitory effect of the light group was as follows: OCZCH+ > CZCH+ > Ce6+ > Control+. The statistical difference between the CZCH+ and Ce6+ groups ($p < 0.05$) indicates that loading into ZIF-8 reduced Ce6 aggregation. The PDT antibacterial action was then greatly improved by the addition of oxygen, as seen by the statistical difference between the OCZCH+ and CZCH+ groups ($p < 0.01$).

Bacteria in biofilms tend to play a stronger pathogenic role. The inhibitory effect of each treatment group on the biofilm formation of *S. mutans* and the eradication effect on mature biofilms were then explored by colony-forming unit (CFU) counting (Fig. 4c and d). Under near-infrared light, OCZCH reduces the bacterial CFU by approx. 2.8 log. From Fig. 4d, it can be intuitively observed that the number of colonies decreases sharply. Upon interacting with negatively charged surface molecules and polysaccharides in the extracellular matrix of the biofilm, the crystalline violet dye causes the *S. mutans* biofilm to take on a dark purple colour which can be observed by the naked eye and quantified by the OD_{600} (Fig. 4e and g).[33] The results showed that there was no statistical difference ($p > 0.05$) between the dark treatment group and the Control+ group, which indicates that light alone or co-culture with Ce6, CZCH, and OCZCH had no inhibitory effect. Intact stained biofilms can be observed in Fig. 4g. After light exposure, the stained biofilm gradually disappeared and only a few purple spots were observed in the OCZCH group. Quantitative detection of crystalline violet provides data-driven visual trends. As shown in Fig. 4e, the OCZCH+ group could reduce biofilm formation by 84.7% and had a strong ability to inhibit the biofilm formation. The results of biofilm activity and the MTT assay showed a similar trend.

The EPS secreted by *S. mutans* in the extracellular polymer of plaque biofilm overlies the bacteria of the biofilm as a protector, resulting in difficulty in removing the biofilm. In this study, EPS was determined by the phenol–sulfuric acid

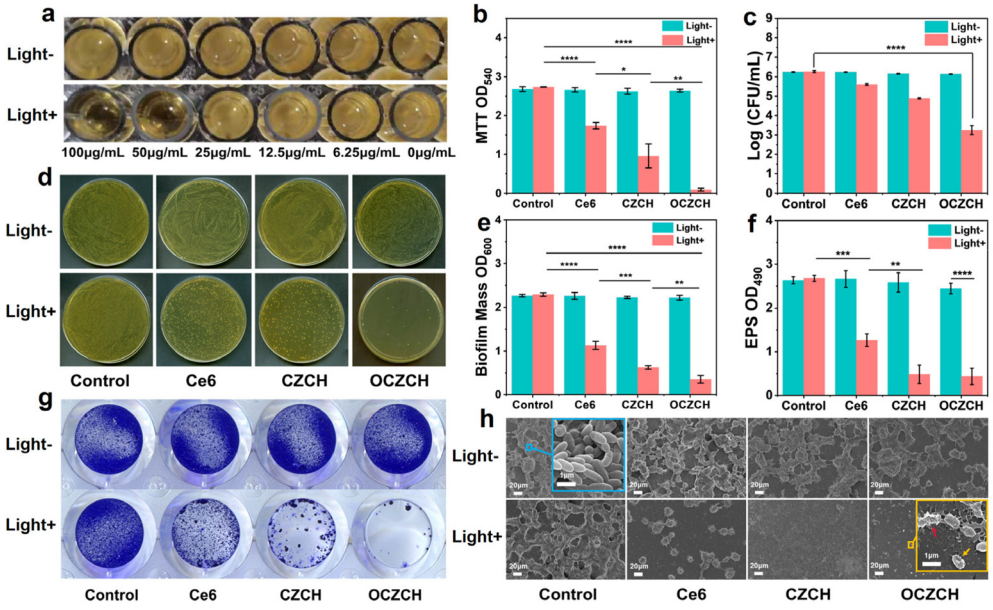

Fig. 4 (a) Minimum inhibitory concentration. (b) MTT assay reflects that the metabolic activity of the *S. mutans* biofilm was evaluated according to the OD_{540} value. (c and d) Bacterial colony plate counting of *S. mutans* and the corresponding quantitative analysis. (e and g) Crystal violet staining measuring the biomass of a multi-species biofilm. (f) The phenol–sulphuric acid method to determine the EPS in extracellular polymers of the *S. mutans* plaque biofilm. (h) SEM images of *S. mutans*, where the yellow arrow indicates the appearance of wrinkled depressions on the surface of the bacteria and the red arrow indicates the presence of more nanoparticles on and around the bacterial surface. $n = 3$, *$p < 0.05$, **$p < 0.01$, ***$p < 0.001$, ****$p < 0.0001$, (t-test). ns, not significant.

method. Fig. 4f shows that the Control+ group and the dark-treated groups hardly inhibit the production of EPS by *S. mutans*. In the meantime, the CZCH+ group further inhibited the EPS production of *S. mutans* compared to the Ce6+ group. The result implies that as a Ce6 and oxygen nanocarrier, ZIF-8 overcomes the problem of agglomeration of photosensitizers. Furthermore, O_2 improves the PDT effect, and the substantial reduction in EPS production in the OCZCH+ group was statistically significant ($p < 0.001$) compared to the CZCH+ group. The inhibitory effect on biofilm metabolic activity was similar to the tendency of biofilm formation in all groups under irradiation conditions. The metabolic activity of the OCZCH+ group was only 16.3%, indicating that OCZCH significantly reduced the metabolic activity of *S. mutans* under near-infrared illumination at 650 nm. The sharp reduction of EPS could reduce the adhesion of *S. mutans* on the tooth surface, thus effectively inhibiting the biofilm formation, explaining why the material reduced the cariogenic toxicity of *S. mutans*.

To further visualize the damaging effect of nanoparticles on *S. mutans* and its biofilm, we observed *S. mutans* after light and dark treatments by SEM. When magnified 1000 times (Fig. 4h), the dark-treated and Control+ groups showed an intact biofilm structure with a thicker and denser biofilm, and the bacteria were surrounded by a large amount of extracellular matrix. The group treated with Ce6+ showed a significant reduction in both the thickness and the density of the biofilm, resulting in the loss of its structural integrity. However, connectivity was still observed between bacteria and extracellular polymer encapsulation. The biofilm of *S. mutans* in the OCZCH+ group was sparse, and exudation was visible due to the breakage of the cell membrane. The yellow arrow in Fig. 4h indicates the appearance of wrinkled depressions on the surface of the bacteria. At the same time, the red arrow indicates the presence of more nanoparticles on and around the bacterial surface, which is the root cause of the collapse of the OCZCH structure.

Live/dead staining of the biofilm was photographed by confocal laser scanning microscopy (CLSM), and live bacteria were stained with green fluorescence (SYTO 9). Dead bacteria with damaged cell membranes were stained in red (PI), resulting in a red fluorescence. The CLSM images of the dark-treated group (Fig. 5a) and the light-only group (Fig. 5b) show that the mature biofilm is thick and dense and that the entire biofilm contains large areas of green fluorescence (live bacteria) and almost invisible red fluorescence (dead bacteria). After 5 min of laser irradiation at 650 nm, the green fluorescence density in the Ce6+ group greatly reduced, and the proportion of red fluorescence increased and partly appeared yellow, which indicated that the Ce6+ group had some antibacterial effects. The CZCH+ group had a sparse amount of biofilm and showed a large area of yellow-orange colour. The bacteria in the biofilm of the OCZCH+ group were sporadically distributed, the red fluorescence dominated, and the antibacterial effect was obvious. These survival patterns and distributions of bacteria were consistent with the results of previous experiments, and the OCZCH+ group still showed the best antibacterial effect.

OCZCH inhibits bacterial acid production and maintains microenvironment stability

The persistent secretion of acid by *S. mutans* decreases the pH value of the surrounding environment to below the critical value for demineralization. At this acidic level, continuous demineralization of tooth enamel occurs and caries develop gradually. However, during the occurrence and development of dental caries, *S. mutans* not only exhibits the ability to secrete cariogenic acid but also shows remarkable acid resistance and the sustained production of acid. Therefore, the acid-producing ability of *S. mutans* is the key to verifying the pathogenicity of bacteria.[34] For this study, the changes in the pH value

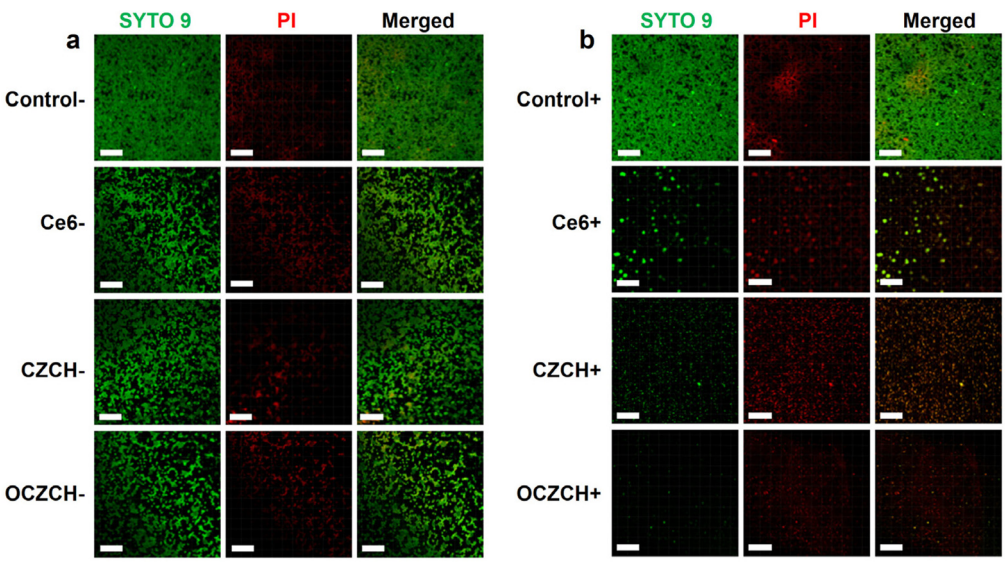

Fig. 5 The confocal laser scanning microscopy images of (a) the dark treatment group and (b) the light illumination group. (scale bars = 100 μm).

Table 1 Effects of Control, Ce6, CZCH, and OCZCH on the pH of the bacterial broth of *S. mutans* under light and dark treatments. Values are presented as mean ± standard deviation. Statistical differences for each group are indicated by single, double or triple asterisk symbols ($p < 0.05$)

Group	pH_0 (0 h)	pH_{24} (24 h)	Δ pH
Control+	7.280 ± 0.035	4.147 ± 0.009	3.133 ± 0.030
Ce6+	7.313 ± 0.015	6.003 ± 0.266	1.310 ± 0.270**
CZCH+	7.273 ± 0.015	6.643 ± 0.090	0.630 ± 0.098*,***
OCZCH+	7.287 ± 0.026	6.893 ± 0.023	0.394 ± 0.041*,***
Control−	7.307 ± 0.030	4.157 ± 0.015	3.150 ± 0.031
Ce6−	7.310 ± 0.017	4.153 ± 0.026	3.157 ± 0.009
CZCH−	7.327 ± 0.023	4.203 ± 0.022	3.124 ± 0.018
OCZCH−	7.297 ± 0.022	4.187 ± 0.028	3.110 ± 0.025

correspond to the antibacterial performance of each experimental group.

As shown in Table 1, after 24 h of incubation, the pH of the Control− group decreased from 7.307 ± 0.030 to 4.157 ± 0.015, with a ΔpH of 3.150 ± 0.031. Meanwhile, there was almost no change in pH between the Control+ and dark-treated experimental groups ($p > 0.05$). These results demonstrate that neither light alone nor drug alone had a significant inhibitory effect on acid production in *S. mutans*. In contrast, the ΔpH of the OCZCH+ group was only reduced by 0.394 ± 0.041, indicating that the acid production capacity of *S. mutans* was greatly reduced by OCZCH under light irradiation. The acid production inhibition rates of the Ce6+, CZCH+, and OCZCH+ groups were 58.2%, 79.9%, and 87.4%, respectively. All experimental groups exhibited acid inhibition ability according to the acid inhibition rate equation. The OCZCH+ group exhibited the best acid inhibition effect among all the experimental groups, thus confirming that OCZCH is the most effective material for bacterial inhibition. The reduction of organic acids in the biofilm resulted in *S. mutans* being unable to provide a favourable growth environment for other bacteria, which inhibited biofilm formation to a certain extent.

Experimental details

Chemicals and materials

Methylimidazole ($C_4H_6N_2$, 2-MI), zinc nitrate hexahydrate ($Zn(NO_3)_2{\cdot}6H_2O$), copper nitrate trihydrate ($Cu(NO_3)_2{\cdot}3H_2O$), 1,3-diphenylisobenzofuran (DPBF), and 3-(4,5-dimethylthiazol-2-yl)-2,5-diphenyltetrazolium bromide (MTT) were provided by Shanghai Aladdin Bio-Chem Technology Co., Ltd. Chlorin e6 (Ce6) was purchased from Shanghai TCI Co., Ltd. Hyaluronic acid (HA) was bought from Shanghai Maclin Biochemical Technology Co., Ltd. Methyl alcohol, ethyl alcohol, and absolute ethyl alcohol were obtained from General-Reagent, China. The CCK-8 kit was purchased from the Tongren Institute of Chemistry, Japan. Brain heart infusion (BHI), agar, sucrose, 0.25% Trypsin/EDTA, and Dulbecco's Modified Eagle's Medium (DMEM) were supplied by Dalian Meilun Biotech Co., Ltd. 2.5% (w/w) glutaraldehyde and phosphate-buffered saline (PBS) were purchased from Solarbio. All the chemical reagents were of analytical grade and used without further purification. Deionized water was used throughout the experiments.

Instruments

Transmission electron microscopy (TEM) images were recorded using an FEI Tecnai G2 F20. Energy-dispersive X-ray spectrometry analysis of nanoparticles was performed on the same TEM instrument with an attached energy-dispersive X-ray spectrometry probe. Scanning electron microscopy (SEM) was conducted using a Zeiss Sigma 300 instrument (Germany). The UV–vis absorption spectra were recorded using a U-3310 UV–vis spectrophotometer. Powder X-ray diffraction (XRD) patterns and X-ray photoelectron spectra (XPS) were recorded using a D8 Advance instrument with Cu Kα radiation and a Thermo Escalab 250Xi, respectively. Surface zeta potential experiments were conducted on a Zetasizer Nano (Malvern). An automatic volumetric adsorption apparatus (Autosorb IQ) was used to measure the oxygen adsorption isotherm (bath temp.: 298k) and record the nitrogen adsorption/desorption curves (bath temp.: 77k), respectively.

Synthesis of OCZCH NPs

O_2-Cu/ZIF-8@Ce6/ZIF-8 (OCZC) NPs were synthesized and modified according to previous reports.[25] In brief, 2-MI (0.660 g) was dissolved in 11 mL of methanol solution. Zn $(NO_3)_2{\cdot}6H_2O$ (0.223 g) and $Cu(NO_3)_2{\cdot}3H_2O$ (0.060 g) were dissolved in 11 mL of methanol solution. Next, the above two solutions were mixed and stirred at room temperature for 1 h. The products (Cu/ZIF-8) were collected by centrifugation (8000 rpm, 7 min) and washed with methanol solution three times. The Cu/ZIF-8 obtained was vacuum-dried overnight in a vacuum-drying oven to remove methanol from the nanoparticles' pores and to facilitate the adsorption of oxygen in the next step.

After that, Cu/ZIF-8 nanoparticles were stirred in an oxygen atmosphere for 3 days to finally obtain O_2-Cu/ZIF-8 (OZC). O_2-Cu/ZIF-8 (20 mg) and Ce6 (2 mg) were dissolved in 10 mL of 2-MI solution (0.01 mol L^{-1} in methanol solution) and stirred under dark conditions for 5 min at room temperature. Then it was mixed with 10 mL of $Zn(NO_3)_2{\cdot}6H_2O$ solution (0.01 mol L^{-1} in methanol solution). Upon stirring at room temperature under dark conditions, the solution became dark green quickly. After 2 h, the ZIF-8 shell containing Ce6 was coated on O_2-Cu/ZIF-8 successfully, and then O_2-Cu/ZIF-8@Ce6-ZIF-8 (OCZC) nanoparticles were collected by centrifugation.

Finally, HA aqueous solution (1 mg mL^{-1}) and OCZC aqueous solution (2 mg mL^{-1}) were mixed and stirred for 3 h. After the reaction, 1/10 volumes of ethanol were added before centrifugation, and then the final products O_2-Cu/ZIF-8@Ce6/ZIF-8@HA (OCZCH) were collected by centrifugation (12 000 rpm, 20 min).

Conclusions

In summary, this study established an excellent acid-responsive, oxygen-carrying antibacterial photosensitive O_2-Cu/ZIF-8@Ce6/ZIF-8@HA (OCZCH). When exposed to 650 nm light, the bio-safety nanocarrier OCZCH exhibits strong antibacterial properties and effectively inhibits oral biofilms through the synergistic effects of Ce6-released ROS supplemented by the carried oxygen. The metabolic and acid-producing capacities of both *Streptococcus mutans* and its biofilms are significantly reduced. OCZCH provides a novel antibiotic-free strategy for the non-invasive and efficient treatment of cariogenic bacterial infections. The effectiveness of OCZCH for the treatment of dental caries is expected to be confirmed through further animal and clinical experiments.

Conflicts of interest

There are no conflicts to declare.

Acknowledgements

This work is financially supported by the National Natural Science Foundation of China (Grant No. NSFC 51972138 and 52272282).

References

1 R. H. Selwitz, A. I. Ismail and N. B. Pitts, *Lancet*, 2007, **369**, 51–59.
2 W. G. Wade, *Pharmacol. Res.*, 2013, **69**, 137–143.
3 Y. Liu, S. G. Daniel, H.-E. Kim, H. Koo, J. Korostoff, F. Teles, K. Bittinger and G. Hwang, *Microbiome*, 2023, **11**, 123.
4 N. Pitts, D. Zero, P. Marsh, K. Ekstrand, J. Weintraub, F. Gomez, J. Tagami, S. Twetman, G. Tsakos and A. Ismail, *Nat. Rev. Dis. Primers*, 2017, **3**, 17030.
5 C. W. Hall and T. F. Mah, *FEMS Microbiol. Rev.*, 2017, **41**, 276–301.
6 M. Liu, L. Huang, X. Xu, X. Wei, X. Yang, X. Li, B. Wang, Y. Xu, L. Li and Z. Yang, *ACS Nano*, 2022, **16**, 9479–9497.
7 Y. Lin, J. Chen, X. Zhou and Y. Li, *Crit. Rev. Microbiol.*, 2021, **47**, 667–677.
8 L. Zhang, Q.-L. Li and H. M. Wong, *Composites, Part B*, 2022, **233**, 109651.
9 Y. Xu, Y. You, L. Yi, X. Wu, Y. Zhao, J. Yu, H. Liu, Y. Shen, J. Guo and C. Huang, *Bioact. Mater.*, 2023, **20**, 418–433.
10 C. A. Arias and B. E. Murray, *N. Engl. J. Med.*, 2009, **360**, 439–443.
11 M. P. Brynildsen, J. A. Winkler, C. S. Spina, I. C. MacDonald and J. J. Collins, *Nat. Biotechnol.*, 2013, **31**, 160–165.
12 B. Yang, Y. Chen and J. Shi, *Chem. Rev.*, 2019, **119**, 4881–4985.
13 M. Piksa, C. Lian, I. C. Samuel, K. J. Pawlik, I. D. W. Samuel and K. Matczyszyn, *Chem. Soc. Rev.*, 2023, **52**, 1697–1722.
14 I. K. Bae, J.-Y. Shin, J.-H. Son, K.-K. Wang and W.-S. Han, *Photodiagn. Photodyn. Ther.*, 2022, **39**, 102975.
15 F. Cieplik, D. Deng, W. Crielaard, W. Buchalla, E. Hellwig, A. Al-Ahmad and T. Maisch, *Crit. Rev. Microbiol.*, 2018, **44**, 571–589.
16 T. Xie, Y. Qi, Y. Li, F. Zhang, W. Li, D. Zhong, Z. Tang and M. Zhou, *Bioact. Mater.*, 2021, **6**, 3812–3823.
17 C. Qin, N. Tang, Y. Gan, H. Zhao, Y. Li, G.-b. Tian, Y. Y. Yang, P. Yuan and X. Ding, *Adv. Healthcare Mater.*, 2023, **12**, 2202903.
18 X. Hu, H. Tian, W. Jiang, A. Song, Z. Li and Y. Luan, *Small*, 2018, **14**, 1802994.
19 X. Fu, Z. Yang, T. Deng, J. Chen, Y. Wen, X. Fu, L. Zhou, Z. Zhu and C. Yu, *J. Mater. Chem. B*, 2020, **8**, 1481–1488.
20 Y. Liu, H. Wu, S. Wang, X. Zhang, L. Gong, C. Xiao, C. Liu, L. Chen, H. Zhao, C. Liu, M. Jin, Z. Gao and W. Huang, *Mater. Today*, 2023, **68**, 125–147.
21 P. Li, J. Li, X. Feng, J. Li, Y. Hao, J. Zhang, H. Wang, A. Yin, J. Zhou, X. Ma and B. Wang, *Nat. Commun.*, 2019, **10**, 2177.
22 H. Zhang, Q. Li, R. Liu, X. Zhang, Z. Li and Y. Luan, *Adv. Funct. Mater.*, 2018, **28**, 1802830.
23 J. Liu, D. Wu, N. Zhu, Y. Wu and G. Li, *Trends Food Sci. Technol.*, 2021, **109**, 413–434.
24 A. Schejn, A. Aboulaich, L. Balan, V. Falk, J. Lalevée, G. Medjahdi, L. Aranda, K. Mozet and R. Schneider, *Catal. Sci. Technol.*, 2015, **5**, 1829–1839.
25 Z. X. Xie, S. Liang, X. C. Cai, B. B. Ding, S. S. Huang, Z. Y. Hou, P. A. Ma, Z. Y. Cheng and J. Lin, *ACS Appl. Mater. Interfaces*, 2019, **11**, 31671–31680.
26 W. Li, X. Zhou, S. Liu, J. Zhou, H. Ding, S. Gai, R. Li, L. Zhong, H. Jiang and P. Yang, *ACS Appl. Mater. Interfaces*, 2021, **13**, 50760–50773.
27 M. S. Usman, M. E. El Zowalaty, K. Shameli, N. Zainuddin, M. Salama and N. A. Ibrahim, *Int. J. Nanomed.*, 2013, **8**, 4467–4479.
28 A. Kumar, A. Sharma, Y. Chen, M. M. Jones, S. T. Vanyo, C. Li, M. B. Visser, S. D. Mahajan, R. K. Sharma and M. T. Swihart, *Adv. Funct. Mater.*, 2021, **31**, 2008054.
29 L. Ding, X. Lin, Z. Lin, Y. Wu, X. Liu, J. Liu, M. Wu, X. Zhang and Y. Zeng, *ACS Appl. Mater. Interfaces*, 2020, **12**, 36906–36916.
30 Y. Song, S. Han, S. Liu, R. Sun, L. Zhao and C. Yan, *ACS Appl. Mater. Interfaces*, 2023, **15**, 25339–25353.
31 Q. Sun, H. Bi, Z. Wang, C. Li, X. Wang, J. Xu, H. Zhu, R. Zhao, F. He, S. Gai and P. Yang, *Biomaterials*, 2019, **223**, 119473.
32 H. Zhang, K. Liu, S. Li, X. Xin, S. Yuan, G. Ma and X. Yan, *ACS Nano*, 2018, **12**, 8266–8276.
33 H. Qiu, F. Pu, Z. W. Liu, Q. Q. Deng, P. P. Sun, J. S. Ren and X. G. Qu, *Small*, 2019, **15**, 1902522.
34 K. Cheng, P. She, H. Wang, Z. Wang, L. Zhang, X. Tang, L. Yuan, Y. Feng, X. Song, G. Pan, J. Yang and L. Liu, *Mater. Horiz.*, 2023, **10**, 512–523.